**Acta Cryst A**

FOUNDATIONS
ADVANCES

# Small-angle X-ray Scattering Tensor Tomography: Model of 3D Reciprocal-Space Map, Reconstruction Algorithm, and Angular Sampling Requirements

**Marianne Liebi\*, Marios Georgiadis, Joachim Kohlbrecher, Mirko Holler, Jörg Raabe, Ivan Usov, Andreas Menzel, Philipp Schneider, Oliver Bunk and Manuel Guizar-Sicairos**

**Category:** *research papers*

**Contact author:**

*Marianne Liebi*

*MAXIV Laboratory, Lund University, P.O. Box 118, Lund, 221 00, Sweden*

*Telephone: +46725682426*

*Fax: ?*

*Email: marianne.liebi@maxiv.lu.se*

1

# Small-angle X-ray Scattering Tensor Tomography: Model of 3D Reciprocal-Space Map, Reconstruction Algorithm, and Angular Sampling Requirements

Marianne Liebi,[a,b,c]* Marios Georgiadis,[d,e] Joachim Kohlbrecher,[a]

Mirko Holler,[a] Jörg Raabe,[a] Ivan Usov,[a] Andreas Menzel,[a]

Philipp Schneider,[f] Oliver Bunk[a] and Manuel Guizar-Sicairos [a]*

[a]*Paul Scherrer Institut, 5232 Villigen PSI Switzerland,* [b] *MAX IV Laboratory, Lund*

*University, 221-00 Lund Sweden,* [c]*Department of Physics, Chalmers University of*

*Technology, 41296 Gothenburg, Sweden,* [d]*Institute for Biomedical Engineering, ETH*

*and University Zurich, 8093 Zurich Switzerland,* [e]*Current address: Center for*

*Biomedical Imaging, New York University School of Medicine, NY 10016, USA, and*

[f]*Bioengineering Science Research Group, Faculty of Engineering and the*

*Environment, University of Southampton, Southampton SO17 1BJ UK.*

*E-mail: marianne.liebi@chalmers.se, manuel.guizar-sicairos@psi.ch*

*(Received 0 XXXXXXX 0000; accepted 0 XXXXXXX 0000)*

## Abstract

Small-angle X-ray scattering tensor tomography, which allows reconstruction of the local 3D reciprocal-space map within a 3D sample as introduced by Liebi *et al.* (2015), is described in more detail with regard to the mathematical framework and the optimization algorithm. For the case of trabecular bone samples from vertebra it is shown that the model of 3D reciprocal-space map using spherical harmonics can adequately

2

describe the measured data. The method enables the determination of nanostructure orientation and degree of orientation as demonstated previously in a single momentum transfer $q$ range. Here we show a reconstruction of the complete reciprocal-space map for the case of bone over extended ranges of $q$. In addition, it is shown that uniform angular sampling and advanced regularization strategies help to reduce the amount of data required.

## 1. Introduction

Nanoscale features can be probed in a spatially resolved fashion when scanning a sample through a focused X-ray beam and recording a small-angle X-ray scattering (SAXS) pattern at each location (Fratzl *et al.*, 1997), a technique referred to as scanning SAXS. The real-space resolution is defined by the beam size and the scanning step size typically chosen in the order of several to a few tens of micrometers, but can also be as small as some tens of nanometers or as large as millimeters. For each scanning point, nanoscale features are probed in reciprocal-space by the SAXS pattern, typically measuring a spectrum of feature sizes in the range of a few nanometers to a few hundred nanometers. The capability of studying the distribution of nanoscale structures over extended sample areas is of particular interest for hierarchically structured materials for which the length scales of interest span many orders of magnitude (Fratzl & Weinkamer, 2007; Meyers *et al.*, 2008; Beniash, 2011; He *et al.*, 2015; Van Opdenbosch *et al.*, 2016).

A two-dimensional (2D) SAXS pattern contains statistical information about the nanostructure within the illuminated sample volume. If a main direction of orientation of the nanostructure exists, it can be determined in a model-independent way. Since a single SAXS pattern probes only a 2D section through the three-dimensional (3D)

3

reciprocal-space, it provides incomplete information if the nanostructure is anisotropic in 3D. The 3D orientation can be retrieved from thin sections of a sample by measuring SAXS patterns at different rotation angles as illustrated in Fig. 1a (Liu *et al.*, 2010; Seidel *et al.*, 2012; Georgiadis *et al.*, 2015). To measure three-dimensional samples without sectioning, scanning SAXS has to be combined with computed tomography (CT) techniques. If the scattering is invariant with respect to sample rotation (Feldkamp *et al.*, 2009), measurements taken at different angles for one rotation axis are enough and standard reconstruction algorithm, such as filtered back-projection or simultaneous algebraic reconstruction technique (SART) can be used. Rotational invariance applies for isotropically scattering samples, *i.e.* with no preferred orientation of the nanostructure or for unidirectional orientation of the nanostructure parallel to the rotation axis (Schroer *et al.*, 2006; Feldkamp *et al.*, 2009; Jensen *et al.*, 2011).
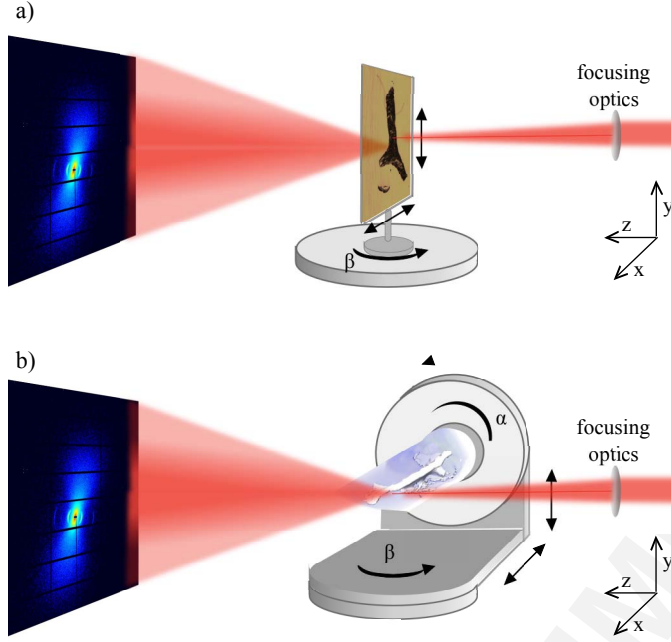
4



Fig. 1. (a) 3D scanning SAXS setup to measure thinly sliced samples. The sample is scanned through the focused beam in $x$ and $y$ at different rotation angles $\beta$ around $y$. (b) SAXS tensor tomography setup to measure 3D samples. The sample is scanned through the focused beam in $x$ and $y$ at $n$ orientations which are described by the rotation matrix $\boldsymbol{R}_n^{\mathrm{exp}}(\alpha, \beta)$.

Skjonsfjell *et al.* (2016) have shown that with strict assumptions on the sample, the orientation distribution can be retrieved from measurements using a single rotation axis by fitting a model of the X-ray scattering to the experimental SAXS pattern. For more general anisotropically oriented scatterers, SAXS acquisition using two rotation axes are needed (see Fig. 1b) in order to retrieve the full 3D reciprocal-space map (Liebi *et al.*, 2015; Schaff *et al.*, 2015). Schaff *et al.* (2015) has extended the concept of the rotation invariance (Feldkamp *et al.*, 2009), by the introduction of virtual tomographic axes. After sorting the 2D SAXS patterns acquired at different rotations around two axes into over a thousand virtual tomography axes, standard reconstruction algorithms, here SART, are used to reconstruct the scattering parallel to each virtual tomographic axis independently.

5

Liebi *et al.* (2015) introduced a method based on the modeling of the 3D reciprocal-space map of each voxel, *i.e.* volume element, using spherical harmonics and minimizing the error between the measured and modeled intensity by an optimization algorithm. The reconstruction contains in each voxel not only a scalar value, such as the X-ray attenuation coefficient in standard CT, but a tensor representing the reciprocal-space map, thus the method is referred to as SAXS tensor tomography. We present here in more detail the mathematical framework of SAXS tensor tomography, as introduced by Liebi *et al.* (2015) and the experimental validation of the model demonstrated on trabecular bone samples. We further investigate the angular sampling and the number of projections required for the reconstruction. In addition, some advanced regularization strategies are introduced and discussed, which reduce the amount of data and measurement time needed.

## 2. Model of scattering signal using a 3D reciprocal-space map

The *ab initio* characterization of the anisotropy of nanostrucure in a 3D volume requires measuring the sample from many possible orientations, not only around one rotation axis, but in a grid of 2D orientation angles using two rotation axes. It is required to define a coordinate transformation from laboratory coordinates $\mathbf{r} = (x, y, z)^T$, with $z$ pointing along the direction of the X-ray beam, to sample Cartesian coordinates $\mathbf{r}'$, as illustrated in Fig. 2. This transformation is described for the $n$-th sample orientation by a rotation matrix $\mathbf{r}' = \boldsymbol{R}_n^{\mathrm{exp}}\mathbf{r}$.

$$\mathbf{r} = \begin{pmatrix} x \\ y \\ z \end{pmatrix} \qquad \mathbf{r}' = \boldsymbol{R}_n^{\mathrm{exp}} \mathbf{r} = \begin{pmatrix} x' \\ y' \\ z' \end{pmatrix} \qquad \hat{\mathbf{u}}^{\mathrm{str}}_{\theta_{\mathrm{op}},\phi_{\mathrm{op}}}(\mathbf{r}',q')$$
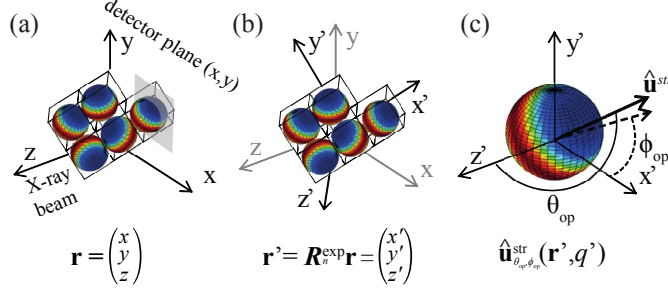
Fig. 2. (a) Laboratory coordinate system $\mathbf{r}$, and (b) object coordinate system $\mathbf{r}'$, which are related by the rotation matrix $\boldsymbol{R}_n^{\mathrm{exp}}$. In (a) the planar 2D cut through the reciprocal-space map in the plane of the detector is illustrated in grey. The object coordinate system $\mathbf{r}'$ defines the position of each voxel of the object. (c) In each voxel a series of spherical harmonics functions is used to describe 3D reciprocal-space map, from which the scattering signal can be obtained. The preferential orientation of the nanostructure in each voxel and each $q$ is characterized by a unit vector $\hat{\mathbf{u}}^{\mathrm{str}}_{\theta_{\mathrm{op}},\phi_{\mathrm{op}}}(\mathbf{r}',q')$ defined by the polar $\theta_{\mathrm{op}}(\mathbf{r}',q')$ and azimuthal $\phi_{\mathrm{op}}(\mathbf{r}',q')$ angles.

The reconstruction aims to determine for each object-coordinate voxel, $\mathbf{r}' = (x',y',z')^T$, a 3D reciprocal-space map, $\hat{R}(\mathbf{r}',\mathbf{q}')$, as a function of a reciprocal-space vector $\mathbf{q}' = (q_x',q_y',q_z')^T$. The object-coordinate system can also be described in spherical coordinates $(r',\theta',\phi')$, with $\theta'$ being the polar angle and $\phi'$ the azimuthal angle. In order to reach this objective, the reciprocal-space map is modelled using spherical harmonics $Y_l^m$ of degree $l$ and order $m$ (Jackson, 1999) as

$$\hat{R}(\mathbf{r}',\mathbf{q}') = \left| \sum_{l,m} a_l^m(\mathbf{r}',q') Y_l^m \left( \Theta(\mathbf{r}',q'), \Phi(\mathbf{r}',q') \right) \right|^2, \tag{1}$$

where $q' = |\mathbf{q}'|$ is the magnitude of the reciprocal-space vector, $a_l^m(\mathbf{r}',q')$ are the spherical harmonic coefficients, and $\Theta(\mathbf{r}',q')$ and $\Phi(\mathbf{r}',q')$ are the polar and azimuthal angles, respectively, which are arguments of the spherical harmonic function. The square of the sum is used to avoid non-physical negative intensities. Since spherical harmonics form a complete basis, higher orders can be used to model the scattering of arbitrarily complex nanostructures. For example, spherical harmonics have been used in texture analysis of pole figures from X-ray diffraction measurements already decades ago (Roe & Krigbaum, 1964; Bunge & Roberts, 1969) using orders up to $l = 36$

7

(Van Houtte, 1983). When reconstructing a scattering model for a large number of voxels of an extended sample however, reducing the number of coefficients and thus minimizing the total number of optimization parameters is of great benefit. For cases where there is a preferential direction of ordering for the nanostructure it is useful to orient the zenith of the spherical harmonics to this direction independently for each voxel in each $q$-range. This results in a sparser representation and reduces the number of coefficients needed to model the reciprocal-space map. This is in particular a good strategy in cases where the 3D reciprocal-space map is not too far from spherical or ellipsoidal symmetry, thus only few components are required in the decomposition of $\hat{R}(\mathbf{r}', \mathbf{q}')$ in equation 1. The local preferential orientation with respect to the object coordinates is characterized by a unit vector, $\hat{\mathbf{u}}^{\text{str}}_{\theta_{\text{op}}, \phi_{\text{op}}}(\mathbf{r}', q')$, as illustrated in Fig. 2c, which is parameterized by the angles $\theta_{\text{op}}(\mathbf{r}', q')$ and $\phi_{\text{op}}(\mathbf{r}', q')$. The arguments of the spherical harmonics, $\Theta(\mathbf{r}', q')$ and $\Phi(\mathbf{r}', q')$ can be implicitly defined by

$$
\begin{pmatrix}
\sin\Theta\cos\Phi \\
\sin\Theta\sin\Phi \\
\cos\Theta
\end{pmatrix} =
$$
$$
\begin{pmatrix}
\cos\theta_{\text{op}}\cos\phi_{\text{op}} & \cos\theta_{\text{op}}\sin\phi_{\text{op}} & -\sin\theta_{\text{op}} \\
-\sin\phi_{\text{op}} & \cos\phi_{\text{op}} & 0 \\
\sin\theta_{\text{op}}\cos\phi_{\text{op}} & \sin\theta_{\text{op}}\sin\phi_{\text{op}} & \cos\theta_{\text{op}}
\end{pmatrix}
$$
$$
\times
\begin{pmatrix}
\sin\theta'\cos\phi' \\
\sin\theta'\sin\phi' \\
\cos\theta'
\end{pmatrix}
$$

$$(2)$$

where $\theta', \phi'$ are the spherical coordinates of the object coordinate system. Neglecting multiple-scattering effects, the contribution of each voxel to the intensity measured at the detector corresponds to a section through the 3D reciprocal-space along the Ewald sphere of radius $2\pi/\lambda$. For the case of small-angle X-ray scattering an expansion of zero order of the Ewald sphere leads to a planar 2D cut through the reciprocal-space map, i.e. $(q_x, q_y, 0)^T$, in the laboratory coordinate Cartesian system as illustrated in Fig.

8

2a. The data in the plane $(q_x, q_y, 0)^T$ corresponds to the $\theta = \pi/2$ plane or $(q, \pi/2, \phi)$ in spherical coordinates. In order to calculate the total intensity at the detector for the $n$-th sample orientation, the contribution from all voxels along the beam path $z$ is summed up,

$$\hat{I}_n(x,y,q,\phi) = \sum_z \left| \sum_{l,m} a_l^m(\mathbf{r}',q) \right.$$
$$\left. \times Y_l^m \left( \Theta(\mathbf{r}',q)|_{\theta=\pi/2}, \Phi(\mathbf{r}',q)|_{\theta=\pi/2} \right) \right|^2 \tag{3}$$

where the measured intensity for the $n$-th sample orientation, $\hat{I}_n$, is a function of the scanning position $(x,y)$.

### 3. Optimization algorithm

For the reconstruction of the 3D reciprocal-space map in one specific $q$-range, an iterative optimization algorithm is used to minimize the error metric $\varepsilon_q$ between the modeled intensity, $\hat{I}_n$ as calculated in equation 3, with respect to the measured data $I_n$, for all scanning positions $(x,y)$ and sample orientations,

$$\varepsilon_q = 2 \sum_{n,x,y,\phi} \omega_n(x,y,q,\phi) \left[ \sqrt{\hat{I}_n(x,y,q,\phi)} - \sqrt{\frac{I_n(x,y,q,\phi)}{T_n(x,y)}} \right]^2 \tag{4}$$

Minimizing this error metric is a first-order approximation to a maximum-likelihood estimation for photon-counting Poisson noise (Thibault & Guizar-Sicairos, 2012). The measured intensity at each point and each orientation is divided by the transmitted intensity $T_n(x,y)$ to compensate for absorption of the sample (Schroer *et al.*, 2006). The parameters to optimize are the spherical harmonic coefficients, $a_l^m(\mathbf{r}',q')$, and their orientation through $\theta_{op}(\mathbf{r}',q')$ and $\phi_{op}(\mathbf{r}',q')$. A binary mask, $\omega_n(x,y,q,\phi)$, is used to denote valid data regions. It is equal to one for all valid data points and can be set to zero for bad detector angular sectors, $\phi$, or where the scattering of the sample is obstructed, for example by the sample mount.

9

To compute $\hat{I}_n$ we first evaluate the sum of the different spherical harmonic terms and compute the modulus squared. The resulting quantity is then projected along the direction of the X-ray beam. The projection operation is calculated using bilinear interpolation. The resulting image is convolved with a $3 \times 3$ pyramidal kernel, which emulates the effect of up- and subsequent down-sampling, to reduce artifacts associated with the discrete volume grid. For the minimization of the error metric, given in equation 4, a conjugate gradient algorithm was used (Press *et al.*, 2007). As the number of optimization parameters is very large, the gradient of the error metric with respect to the optimization parameters is calculated analytically (see Appendix A). In each iteration step the gradient is computed according to equations 10, 11, and 14, followed by a line search in a conjugate direction induced by the local curvature of the function to be optimized (equation 4).
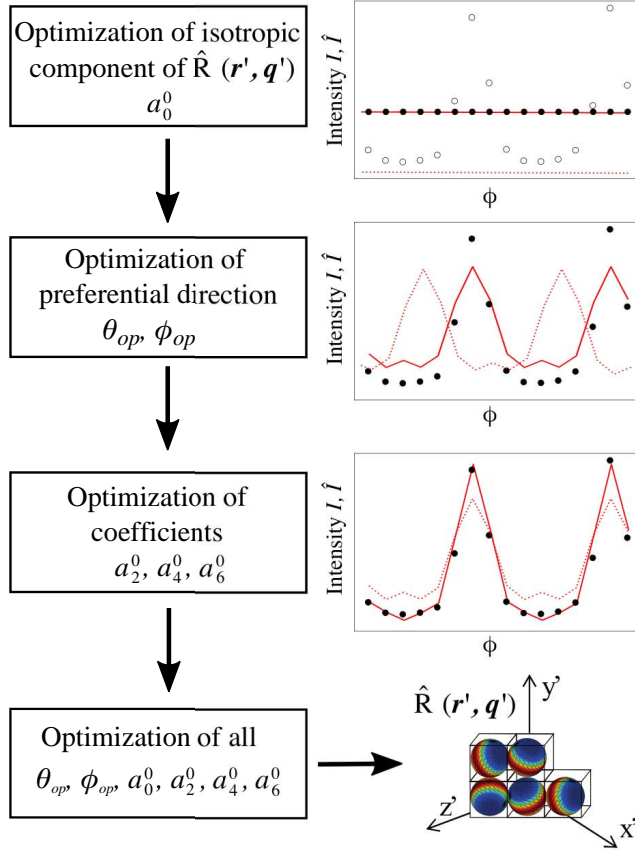
Fig. 3. Flow chart of the optimization procedure. The output of the optimization is for each object coordinate voxel $\mathbf{r}'$ the 3D reciprocal space map $\hat{R}(\mathbf{r}', \mathbf{q}')$ parameterized by the preferential orientation $\hat{\mathbf{u}}_{\theta_{\mathrm{op}}, \phi_{\mathrm{op}}}^{\mathrm{str}}(\mathbf{r}', q')$ and the coefficients of the spherical harmonics $a_l^m(\mathbf{r}', q')$. The optimization is performed in four steps to accelerate convergence. Red dotted lines indicate starting values of the modeled intensity $\hat{I}_n$ in each step, whereas solid red lines indicate the resulting $\hat{I}_n$ after the corresponding optimization step. The measured intensity $I_n$ are shown as black dots, in the first step the optimization is performed using the data averaged over $\phi$.

In order to accelerate convergence, the optimization is performed in four steps as illustrated in Fig. 3. First, the isotropic component of the reciprocal space map $\hat{R}(\mathbf{r}', \mathbf{q}')$ is optimized by using only the isotropic spherical harmonic term with $l = [0]$ and $m = [0]$ and averaging the data over $\phi$. Secondly, only the angles are optimized and the coefficients for $l = [0\,2\,4]$, $m = [0\,0\,0]$ are kept constant at a factor $s$ times the $a_0^0(\mathbf{r}', q')$ obtained in the first step. For the bone measurements shown in this paper

11

the coefficients were set to $s = 1$ for $a_0^0(\mathbf{r}', q')$, $s = -1/3$ for $a_2^0(\mathbf{r}', q')$ and $s = 1/6$ for $a_4^0(\mathbf{r}', q')$. These coefficients were chosen to approximate the anisotropy which was observed in similar samples. Alternatively, symmetries in the 3D reciprocal-space map, which help determining the number of spherical harmonics functions needed, can be estimated from the shape of the scattering object studied. Without previous knowledge of the sample, by repeating the optimization procedure with different constant values of the coefficients in the second step and comparing the results, one can avoid that a solution is obtained which is just a local minimum of the error metric. It is also possible to gain knowledge about the 3D reciprocal-space map by studying a flat sample at different sample rotations as outlined in Section 4. In the third step the coefficients $a_2^0(\mathbf{r}', q')$, $a_4^0(\mathbf{r}', q')$ and $a_6^0(\mathbf{r}', q')$ were optimized while the angles and $a_0^0(\mathbf{r}', q')$ from the first step were kept constant. Finally, in the last step all coefficients and angles were optimized simultaneously.

A support constraint on the object was used in order to optimize only the part of the object 3D grid volume which contains the sample. For this a 3D binary support mask, $M(\mathbf{r}')$, is introduced, denoting with zeros the regions without sample. This can be obtained for example using a threshold after the first optimization step where a first estimate of $a_0^0(\mathbf{r}', q')$ is obtained. The mask, $M(\mathbf{r}')$, is then used when computing the gradients to set the gradients outside the object to zero, as shown in equations 10, 11, and 14. Boundary conditions on the values of the coefficients can be introduced either using constrained optimization algorithms or by introducing a smooth penalty term to the error metric. This can be used for example to enforce symmetries if it is known that they are present in the sample. For example, for the case of $a_l^m(\mathbf{r}', q') > c$

$$\varepsilon_q' = \varepsilon_q + \lambda \varepsilon_q^{(p)} + \mu \varepsilon_q^{(reg)} \tag{5}$$

12

where

$$\varepsilon_q^{(p)} = \sum_{\mathbf{r}'} \begin{cases} \left[a_l^m(\mathbf{r}',q) - c\right]^2, & \text{if } a_l^m(\mathbf{r}',q) < c, \\ 0 & \text{otherwise} \end{cases} \qquad (6)$$

Here $\lambda$ controls the strength of the penalty term. In the reconstructions shown in the manuscript, no such penalty term was used. The regularization term, $\mu\varepsilon_q^{(reg)}$, in equation 5 will be explained in Section 5.2.

## 4. Experimental validation of reciprocal-space model for trabecular bone

To validate the suitability of a series of spherical harmonics as a model to describe the 3D reciprocal-space map, we used data from a $20\,\mu m$ thin section of trabecular bone (sample A). The data were taken with a beam size of $20 \times 20\,\mu m^2$ at different rotation angles $\beta$ around the $y$-axis of the beamline coordinate system as illustrated in Fig. 1a. Further experimental details can be found in Appendix B. As the lateral resolution matches the thickness, the measurements give an adequate representation of imaging a planar arrangement of voxels and it has been shown that for thin samples a single rotation axis provides sufficient information of the 3D arrangement of nanostructures (Georgiadis et al., 2015). Image registration (Guizar-Sicairos et al., 2008) of the transmission images, recorded simultaneously to the SAXS data, was used to assign the scattering from multiple orientations to individual voxels. This procedure is described in more detail in (Georgiadis et al., 2015).
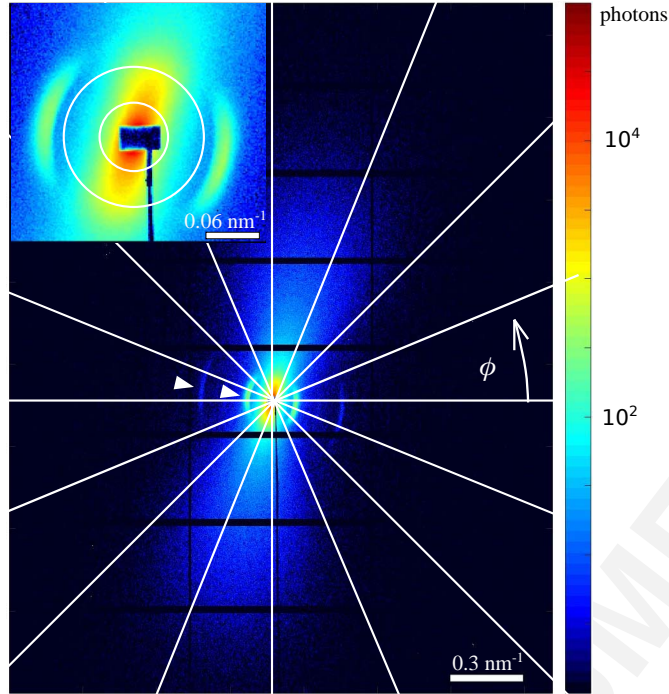
13



Fig. 4. 2D scattering pattern in logarithmic scale obtained from a thin slice of trabecular bone and a zoom-in to the low $q$ range. The 16 segments in which the radial integration is performed are indicated by white lines and two circles that mark a range of $q$-values. White triangles point at the pronounced first and the faint third diffraction orders of mineralized collagen fibers.

Figure 4 shows a single scattering pattern from one scan point of the measurement. Since the nanostructure causing the scattering has a preferential orientation, the recorded SAXS pattern is anisotropic. Furthermore, since the nanostructure anisotropy is three-dimensional, the scattering pattern depends on the sample orientation, $\beta$ (Georgiadis *et al.*, 2015). The scattering from bone originates mainly from the electron density contrast between hydroxyapatite mineral crystal platelets and the surrounding material with lower electron density, such as collagen and water (Fratzl *et al.*, 1997). The main characteristics of the 2D small-angle X-ray scattering signal from bone are the distinct Bragg reflections from the periodic gaps in the collagen fibrils which are filled by hydroxyapatite crystals (Fratzl *et al.*, 1991). The repeat distance of these gaps is approximately 65 nm and they produce characteristic arcs in the scattering pattern

14

(Wilkinson & Hukins, 1999). The first and third harmonic of this signal are indicated by white triangles in Fig. 4. In the direction perpendicular to these arcs a fan-shaped scattering profile can be seen, which arises from the shape, size and lateral arrangement of the mineral platelets in and around the collagen fibrils (Norio *et al.*, 1982). At high $q$-values, $q > 0.125\,\mathrm{nm}^{-1}$, primarily the mineral platelets with approximate size of $3 \times 25 \times 50\,\mathrm{nm}^3$, can be probed. At low $q$-values, $q < 0.1\,\mathrm{nm}^{-1}$, the scattering contains mainly information of the lateral arrangement of the collagen fibrils and the diameter of the fibrils, which is typically in the range of $50 - 200\,\mathrm{nm}$ (Fratzl & Weinkamer, 2007; Gourrier *et al.*, 2010; Pabisch *et al.*, 2013; Giannini *et al.*, 2014). The organization of bone is hierarchical: the orientation of the mineral crystals, the collagen fibrils, the fibril bundles, the fibres, and the macroscopic bone organization are closely related to each other (Rinnerthaler *et al.*, 1999; Fratzl & Weinkamer, 2007; Seidel *et al.*, 2012; Granke *et al.*, 2013; Georgiadis *et al.*, 2015; Georgiadis *et al.*, 2016).
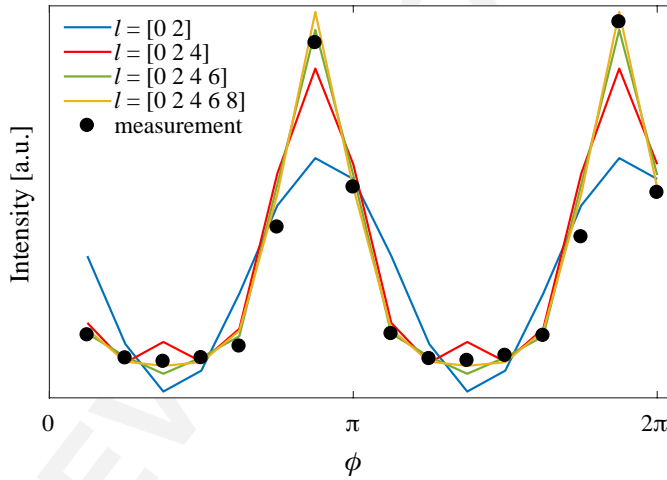


Fig. 5. SAXS measurements from a single voxel for $q = (0.0379 - 0.0758\,\mathrm{nm}^{-1})$ for one sample rotation angle $\beta = 20°$ are shown with black dots. The corresponding modeled data (lines) with different degrees $l$ and zero order $m$ of spherical harmonics are shown as a function of the azimuthal angle $\phi$ in the detector plane.

The intensity of each scattering pattern was integrated in 16 azimuthal segments, shown by white lines in Fig. 4, for each momentum transfer $q$. Increasing the number

15

of azimuthal segments was found to have no significant influence on the results while increasing the amount of data and calculation time. Black dots in Fig. 5 show the measured intensity at the detector versus azimuthal angle $\phi$ in one $q$-range, $0.0379 - 0.0758\,\text{nm}^{-1}$, indicated by concentric circles in Fig. 4 in the 16 azimuthal segments. Symmetries, such as point symmetry, are very common in SAXS and can be easily enforced in our model by choosing the appropriate degrees and orders of the spherical harmonics. For the case of trabecular bone we assume a point symmetry around $q = 0$ and a rotational symmetry around one axis. Thus, using only even degree $l$ and zero order $m$ is enough to model the scattering signal retrieved from the 3D reciprocal-space map. If the mineral platelets did not point in all directions perpendicular to the fibril axis with equal probability, the resulting reciprocal-space map would not be a ring with cylindrical rotational symmetry. For this case in which the rotational symmetry is not given, higher azimuthal orders, $m$, of spherical harmonics are needed to capture this feature. Figure 5 shows for one sample orientation, $\beta = 20°$, the intensity at the detector versus azimuthal angle $\phi$, for the measured and modeled data. The azimuthal orientation of the scattering pattern can already be described well using only degrees $l = [0\,2]$. However the only functional dependence allowed for these small orders is a sine or cosine function (blue line in Fig. 5), which is insufficient to quantitatively model the scattering profile, as can be seen in Fig. 5. Using $l = [0\,2\,4]$ and $m = [0\,0\,0]$ (red line) the sharpness of the peak is not yet described fully, and an artificial increase in the low intensity region appears. Using spherical harmonics of degree $l = [0\,2\,4\,6]$ and order $m = [0\,0\,0\,0]$ (green line) it is possible to reproduce reliably the measured data. Adding yet a higher degree (yellow line) does not improve the model significantly.

Consequently, the model was applied with $l = [0\,2\,4\,6]$ and $m = [0\,0\,0\,0]$ to reconstruct the $q$-resolved 3D reciprocal-space map from the dataset from sample A. The optimization was performed at 32 $q$-values between $0.0303$ and $0.9841\,\text{nm}^{-1}$,

16

each with a radial width of $0.0061\,\mathrm{nm}^{-1}$. Figure 6 shows a good agreement of the fit (points and dashed lines) with the data (solid lines) for the full $q$-range covered by the 2D detector. For selected $q$-values the modeled 3D reciprocal-space map is shown. The characteristic reciprocal-space footprint of the mineral platelets, which appears as a fan-shaped profile in a 2D pattern as seen in Fig. 4, appears in the 3D reciprocal-space map as a ring perpendicular to the direction of the fibril axis and with angular spread related to the fibrils' degree of orientation. This ring can be observed in the whole investigated $q$-range in Fig. 6. The Bragg reflection, which is associated with the collagen periodic gaps, appears in the 3D reciprocal-space map as a cap. It is visible for the first and third harmonic of the reflection (see triangle in Fig. 6). Using $l = [\,0\,2\,4\,6\,]$ and $m = [\,0\,0\,0\,0\,]$ is enough to capture both features typical for the scattering from bone. Reconstructing the full $q$-resolved 3D reciprocal-space map opens up the possibility to retrieve the size and shape of the scattering object from fitting as done in standard small-angle scattering analysis (Bressler $et\ al.$, 2015).
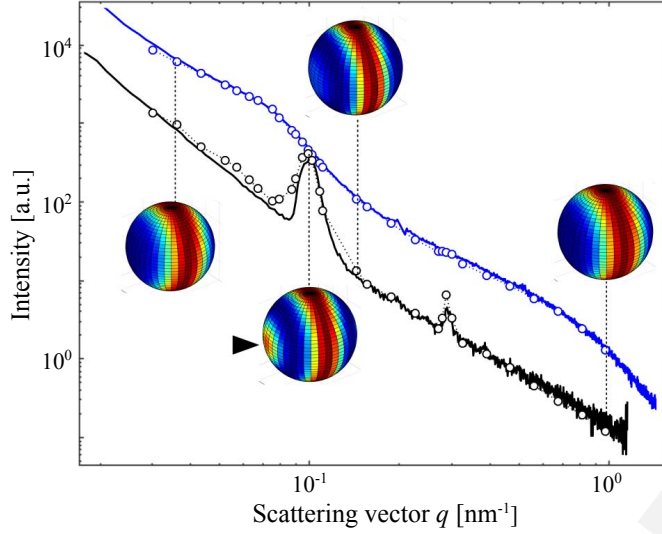
17



Fig. 6. Plots for measured (solid lines) and modeled (circles and dashed lines) intensity
from a single voxel in 2 of the 16 azimuthal segments on the detector plane. The
optimization was performed in 32 $q$-values separately. For some $q$-values the 3D
reciprocal-space maps are shown mapped onto a sphere. A black triangle points
toward the intensity cap characteristic of the 65 nm collagen repeat distance.

## 5. SAXS tensor tomography

In order to extend this method to volumetric samples we combine SAXS with com-
puted tomography. In standard computed tomography a scalar quantity, such as the
sample absorption, is measured for each point within 2D projections and the recon-
struction is three dimensional. In such a case it is sufficient to measure projections at
different sample orientations around a single rotation axis which is perpendicular to
the X-ray beam propagation direction. For the case of SAXS one needs a reconstruc-
tion of the 3D reciprocal-space map for each voxel, as described by the 6D function
in equation 3. Using the principles of invariant scattering along the direction of sam-
ple rotation (Feldkamp *et al.*, 2009), Schaff *et al.* (2015) showed that for an *ab initio*
reconstruction it is sufficient to measure SAXS patterns from all points of the sample,
while sampling object orientations in the full $2\pi$ steradians. To achieve this in the

18

experiment a second rotation axis was introduced as schematically shown in Fig. 1b. Raster scans of the whole sample, here also referred to as projections, are measured at different angles $\alpha$ and different tilt angles of this rotation axis, $\beta$. The object rotation matrix $\boldsymbol{R}_n^{\mathrm{exp}}$ in each sample orientation $n$ can be calculated by a rotation around $y$ by an angle $\beta(n)$ followed by a rotation around $x$ by an angle $\alpha(n)$ resulting in

$$\boldsymbol{R}_n^{\mathrm{exp}}(\alpha, \beta) = \begin{pmatrix} \cos(\beta) & \sin(\alpha)\sin(\beta) & -\cos(\alpha)\sin(\beta) \\ 0 & \cos(\alpha) & \sin(\alpha) \\ \sin(\beta) & -\cos(\beta)\sin(\alpha) & \cos(\alpha)\cos(\beta) \end{pmatrix} \tag{7}$$

Because the sample is not perfectly aligned in the rotation center of both rotation axes, the translational alignment of the measured projections has to be refined. For this purpose an X-ray absorption tomogram is reconstructed from the measured transmission images at $\beta = 0°$, using standard filtered back-projection algorithms. The sample transmission is measured simultaneously to the SAXS pattern using a photo diode mounted on the beamstop, which blocks the direct unscattered beam and avoids damage to the detector. For each object orientation, $(\alpha, \beta)$, a projection from this absorption tomogram was calculated and used as a reference for alignment of the measured transmission images at the corresponding orientation. For this an efficient image registration approach based on selective upsampling of the cross-correlation (Guizar-Sicairos *et al.*, 2008) was used. If the sample has little contrast in the absorption measurement, alternatively the scattering intensity, averaged over $\phi$ in a chosen $q$-range, can be used for this step.

A human trabecular bone cylinder (Sample B, Appendix B) of about $1\,\mathrm{mm}^3$ was measured with a scanning step size in $x$ and $y$ of $25\,\mu\mathrm{m}$. In total $n = 240$ projections, *i.e.* different sample orientations $\boldsymbol{R}_n^{\mathrm{exp}}$, were measured with an angular step of $\Delta\alpha = 4.5°$ between $0°$ to $180°$ and $\Delta\beta = 15°$ between $-30°$ to $45°$. The analysis was carried out following the procedure as described in Section 3 using a $q$-range between $0.0379\,\mathrm{nm}^{-1}$ and $0.0758\,\mathrm{nm}^{-1}$.
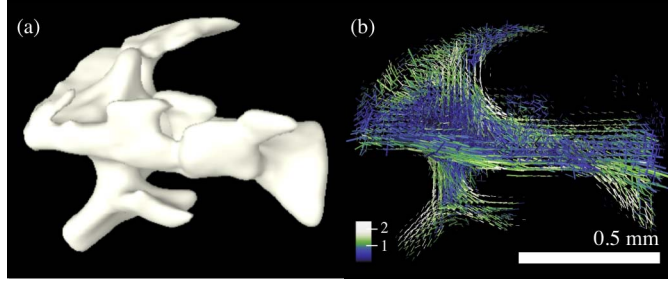
Fig. 7. Human trabecular bone (Sample B). (a) Standard tomographic reconstruction based on the sample X-ray absorption. (b) Orientation of the bone ultrastructure as retrieved from SAXS tensor tomography. Color, length and direction represent degree of orientation, isotropic component $a_0^0$, and main orientation of the collagen fibrils, respectively.

In Fig. 7 the resulting main orientation of the bone ultrastructure is indicated by the direction of cylinders, the strength of the isotropic component $a_0^0$ by the length of cylinders, and the degree of orientation $\rho$ by the color. The later is calculated by the ratio of anisotropic component of $\hat{R}(\mathbf{r}', \mathbf{q}')$ to $\hat{R}(\mathbf{r}', \mathbf{q}')$, namely

$$
\rho(\mathbf{r}', q') = \frac{\int\limits_0^\pi \int\limits_0^{2\pi} \left| \sum_{l=1}^{\infty} \sum_{m=-l}^{l} a_l^m(\mathbf{r}', q') Y_l^m(\Theta, \Phi) \right|^2 \sin(\Theta) \mathrm{d}\Phi \mathrm{d}\Theta}{\int\limits_0^\pi \int\limits_0^{2\pi} \left| \sum_{l=0}^{\infty} \sum_{m=-l}^{l} a_l^m(\mathbf{r}', q') Y_l^m(\Theta, \Phi) \right|^2 \sin(\Theta) \mathrm{d}\Phi \mathrm{d}\Theta}
$$
$$
= \frac{\sum_{l=1}^{\infty} \sum_{m=-l}^{l} |a_l^m(\mathbf{r}', q')|^2}{\sum_{l=0}^{\infty} \sum_{m=-l}^{l} |a_l^m(\mathbf{r}', q')|^2}. \tag{8}
$$

For the reconstruction shown in Fig. 7, 830'000 SAXS patterns were used, which were acquired in 8 h total exposure time and an overall measurement time of 20.3 h including overhead from motor movements. See more details about the measurement in Appendix B. Minimizing measurement time can be tackled by changes in the hardware, *e.g.* reducing motor scanning overhead and faster detectors (Tinti *et al.*, 2015). Another important aspect is to optimize spatial and angular sampling, as discussed in the following section.

20

*5.1. Dependence of reconstruction quality on angular sampling*

In order to study the effect of the angular sampling of object orientations on the reconstruction, the optimization procedure for Sample B was repeated using different subsets of the measured angular projections $n$. Whereas a smaller number of projections are used during these reconstructions, to compare the final quality of the reconstruction Fig. 8 shows the error with respect to all 240 projections. Therefore, the full data set is used as a "gold standard" even when only a subset of the data is available in these test reconstructions. The whole data set is schematically shown in Fig. 8 (in red), where each point on the sphere represents a sample orientation and the measurements at the 6 values for $\beta$ are shown as 6 meridional rows. For comparison, the projections from the full data set have been removed keeping either the original $\Delta\alpha = 4.5°$, (in blue), or $\Delta\beta = 15°$, (in black).
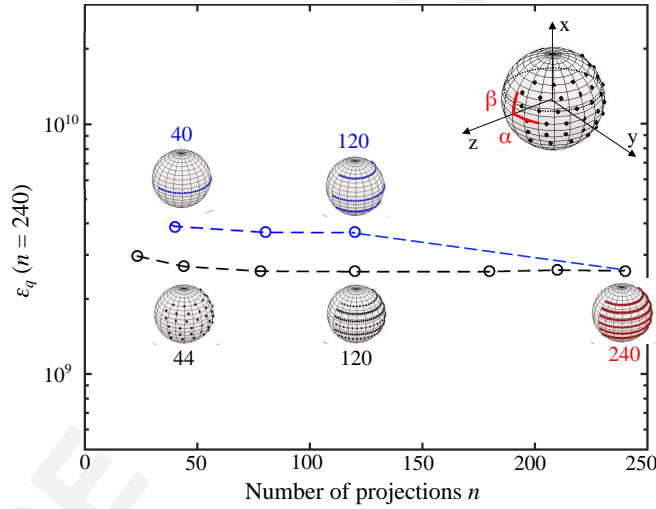


Fig. 8. The error according to equation 4 between the modeled intensity and all measured projections (=240) as a function of the number of projections used in the optimization. The two curves show the error metric for datasets where the projections are reduced by keeping constant either $\Delta\alpha$ (blue) or $\Delta\beta$ (black). The spherical insets show the angular sampling schematically drawn on a sphere, where each object orientation $(\alpha,\beta)$ can be represented by a point on the hemisphere.

21

For the blue curve, we obtain 120 projections by taking a subset of the data corresponding to $\Delta\alpha = 4.5°$ and $\Delta\beta = 30°$. Furthermore, 40 projections were obtained by removing completely the tilt of the rotation angles and keeping $\Delta\alpha = 4.5°$. In contrast, for the curve in black we label the result with 120 projections for which we increased to $\Delta\alpha = 9°$ and kept the original $\Delta\beta = 15°$ and furthermore tested 44 projections by increasing to $\Delta\alpha = 22.5°$ while keeping the original $\Delta\beta = 15°$. That means the 40 projections (in blue) correspond to the sampling along only one rotation axis, similar to standard absorption-based computed-tomography, while the 44 projections (in black) correspond to an almost isotropic angular sampling ($\Delta\alpha \approx \Delta\beta$).

The black curve with a more isotropic angular sampling results in a lower error compared to the corresponding points on the blue curve. The error using 120 projections around 3 tilt angles $\Delta\beta$ of the rotation axis in blue is even higher than for the 44 projection reconstruction with isotropic angular sampling (black), even though the latter has close to 60 percent fewer projections. This difference can be attributed to the angular distribution of these projections, where the 44 projection tomogram has almost isotropic angular sampling in $\alpha$ and $\beta$, and emphasizes the importance of adequate angular sampling of the full hemisphere of sample orientations.

Following the black line it is evident that the error metric with respect to the full dataset remains constant for an extended range of sample rotations $n$, which means that the fit to the complete dataset does not change much by reducing the number of projections even to a fraction close to one third. This indicates that the dataset was taken with significantly more projections than needed. One reason is that the choice of $\Delta\alpha = 4.5°$ was based on the full diameter of the sample, not taking into account any sparsity of the sample, which could reduce angular sampling requirements. The spatial sparsity of the sample is actively used in the tensor tomography reconstruction through the mask $M(\mathbf{r}')$. Another form of sparsity may arise from the fact that

22

the bone ultrastructure exhibits domains in the order of a few hundred microns. In these reconstructions we did not use corresponding constraints. However this domain structure is evident even from the SAXS projections in Fig. 9. In section 5.2 we show an approach how to take advantage of this knowledge through regularization.

As a validation of the reconstruction, the 2D projections from SAXS tensor reconstruction were computed and compared to the data, in other words we compared the measured scanning SAXS data for a projection in a given orientation of the sample, $I_n(x, y, q, \phi)$, with the corresponding projected intensity of the reconstruction, $\hat{I}_n(x, y, q, \phi)$. The first column in Fig. 9 shows a representation of a scanning SAXS projection where the scattering intensity, degree of orientation and main scattering orientation are mapped to the image intensity, color saturation and hue, respectively (Bunk *et al.*, 2009). The color wheel inset relates the direction of the main scattering orientation to the particular hue. As already mentioned it is evident that the trabecular bone sample exhibits domains within which the nanostructure orientation is spatially correlated. The projected intensity of the reconstructions are computed using equation 3 and shown in Fig. 9 for the case of the full dataset ($n = 240$) and for 44 projections. By examining Fig. 9 it can be seen that the experimental projections could be reliably reproduced with as few as $n = 44$ projections for this sample, which would effectively allowed for a reduction to one fifth of the scanning time and the deposited dose.
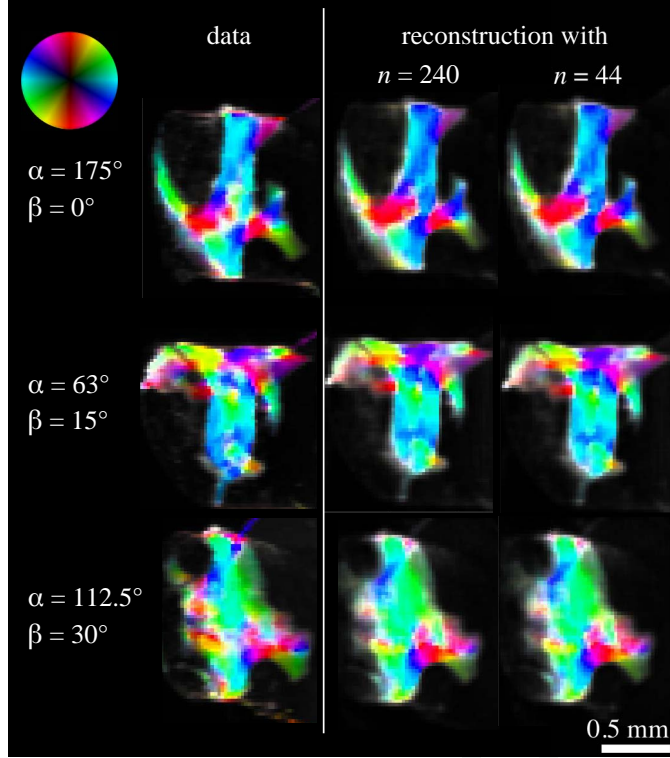
23



Fig. 9. Comparison between measured 2D scanning SAXS projections and the equivalent projection obtained from the reconstruction using subsets of the data corresponding to $n = 240$ and $44$ sample orientations. The color wheel represents the main scattering orientation, the hue the scattering intensity, and the degree of orientation the color saturation.

### 5.2. Regularization strategies

In some cases there is a tendency during a reconstruction to exacerbate high-spatial-frequency noise both in the coefficients $a_l^m(\mathbf{r}', q')$ as well as in the direction $\hat{\mathbf{u}}_{\theta_{\mathrm{op}},\phi_{\mathrm{op}}}^{\mathrm{str}}(\mathbf{r}', q')$. To alleviate this problem a regularization method was implemented. Regularization is often used in optimization to better constrain ill-posed or ill-conditioned problems. The chosen approach for the coefficients follows a method akin to Grenander's method of sieves (Grenander, 1981) by spatially convolving the gradient with respect to the spherical harmonics coefficients (equation 10) with a 3D Hamming window. We use windows of either $3 \times 3 \times 3$ or $5 \times 5 \times 5$ voxels. With this

24

method the optimization solves first for the low and middle spatial frequencies while the high spatial frequencies are introduced last.

For the regularization of the local preferential orientation, $\hat{\mathbf{u}}_{\theta_{\mathrm{op}},\phi_{\mathrm{op}}}^{\mathrm{str}}(\mathbf{r}',q')$, the gradient convolution approach is not suitable because the direction is jointly represented by two parameters, $\theta_{\mathrm{op}}(\mathbf{r}',q')$ and $\phi_{\mathrm{op}}(\mathbf{r}',q')$. In addition, the representation of an orientation using a vector has the inherent ambiguity that $\hat{\mathbf{u}}_{\theta_{\mathrm{op}},\phi_{\mathrm{op}}}^{\mathrm{str}}(\mathbf{r}',q')$ and $-\hat{\mathbf{u}}_{\theta_{\mathrm{op}},\phi_{\mathrm{op}}}^{\mathrm{str}}(\mathbf{r}',q')$ would represent the same local orientation for a reciprocal-space map with a point symmetry. These characteristics do not pair well with a convolution. To penalize spurious variations of the orientation from neighboring voxels a regularization term, $\mu\varepsilon_q^{(reg)}$, to the error metric was introduced in equation 5. The regularization term is based on the absolute value of the dot product between neighboring $\hat{\mathbf{u}}_{\theta_{\mathrm{op}},\phi_{\mathrm{op}}}^{\mathrm{str}}(\mathbf{r}',q')$, namely

$$
\begin{aligned}
\varepsilon_q^{(reg)} = \sum_{\mathbf{r}'} \Big[ & 1 - \Big| \hat{\mathbf{u}}_{\theta_{\mathrm{op}},\phi_{\mathrm{op}}}^{\mathrm{str}}(\mathbf{r}',q) \cdot \hat{\mathbf{u}}_{\theta_{\mathrm{op}},\phi_{\mathrm{op}}}^{\mathrm{str}}(\mathbf{r}'+\hat{i},q) \Big| \\
& + 1 - \Big| \hat{\mathbf{u}}_{\theta_{\mathrm{op}},\phi_{\mathrm{op}}}^{\mathrm{str}}(\mathbf{r}',q) \cdot \hat{\mathbf{u}}_{\theta_{\mathrm{op}},\phi_{\mathrm{op}}}^{\mathrm{str}}(\mathbf{r}'+\hat{j},q) \Big| \\
& + 1 - \Big| \hat{\mathbf{u}}_{\theta_{\mathrm{op}},\phi_{\mathrm{op}}}^{\mathrm{str}}(\mathbf{r}',q) \cdot \hat{\mathbf{u}}_{\theta_{\mathrm{op}},\phi_{\mathrm{op}}}^{\mathrm{str}}(\mathbf{r}'+\hat{k},q) \Big| \Big],
\end{aligned}
\tag{9}
$$

where $\hat{i},\hat{j},\hat{k}$ are the Cartesian coordinate unit vectors, pointing in $x',y',z'$, respectively. $\mu$ is a free parameter that controls the relative strength of the regularization.

The effect of this regularization on the orientation is shown in Fig. 10. A trabecular bone sample (Sample C) of approximately $250\,\mu\mathrm{m}$ diameter was measured with a beam of $5\times1.4\,\mu\mathrm{m}^2$ and a scan step size of $5\,\mu\mathrm{m}$ with a total of 333 angular projections, with an even distribution of projection angles $\Delta\beta = 7.5°$ and $\Delta\alpha = 7.5°\cos(\beta)$ according to the discussion in section 5.1. Fig. 10(a) shows an axial slice through the reconstruction of $\hat{\mathbf{u}}_{\theta_{\mathrm{op}},\phi_{\mathrm{op}}}^{\mathrm{str}}(\mathbf{r}',q)$ without regularization of the direction in which high-spatial-frequency fluctuations of the direction between neighboring voxels are observed. Increasing the value of $\mu$, Figs. 10(b)−(f) demonstrate an increasing smoothness of the reconstruction of $\hat{\mathbf{u}}_{\theta_{\mathrm{op}},\phi_{\mathrm{op}}}^{\mathrm{str}}(\mathbf{r}',q)$.
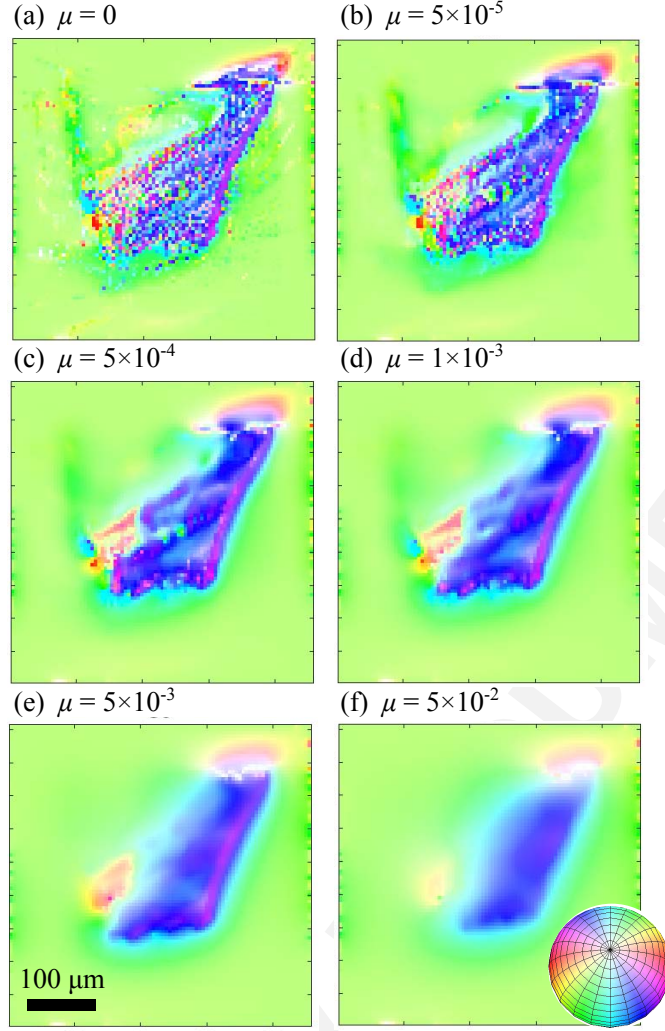
25



Fig. 10. A cross section through the 3D reconstruction of the local orientation, $\hat{\mathbf{u}}^{str}_{\theta_{\mathrm{op}},\phi_{\mathrm{op}}}$, is shown for (a) a reconstruction without regularization and (b)−(f) with different values of the regularization parameter $\mu$. The 3D orientation of $\hat{\mathbf{u}}^{str}_{\theta_{\mathrm{op}},\phi_{\mathrm{op}}}$ was encoded through both hue and saturation, as indicated by the inset color sphere.

In order to select an appropriate regularization parameter $\mu$ the L-curve technique was applied (Hansen, 1992; Li *et al.*, 2003; Belge *et al.*, 2002; Santos & Bassrei, 2007). The L-curve is a plot of the data error, $\varepsilon_q$, versus the regularization penalty term, $\varepsilon_q^{(reg)}$, where each point corresponds to different values of the regularization strength, $\mu$, see Fig. 11a. The corner of the L-curve corresponds to a trade-off between a smooth solution with a high error metric $\varepsilon_q$ and a solution with a small error but more high

26

frequency noise (Hansen, 1992). Figure 11b shows the two terms of the error metric $\varepsilon'_q$ versus the regularization parameter $\mu$. The regularization parameter should be selected around the inflection point combined with a visual quality inspection of the solution (Fig. 10). Here we chose $\mu = 1 \times 10^{-3}$. This point is on the left side corner of the L-curve (red arrow in Fig. 11a) because we prioritize a small error over a smooth solution.


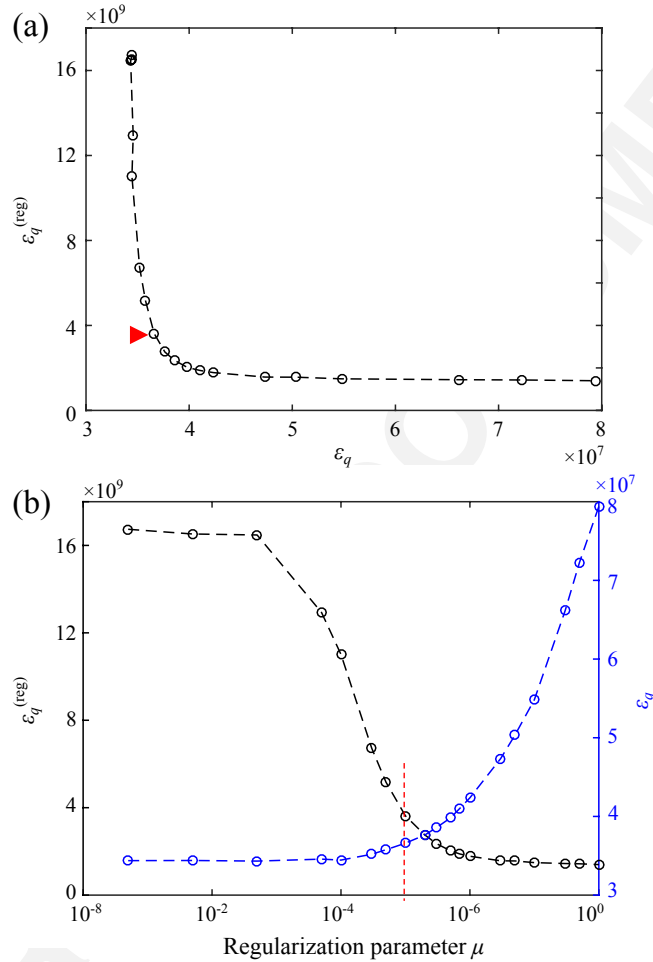
Fig. 11. (a) L-curve used to find an appropriate regularization parameter $\mu$. (b) shows the dependence of the penalty term $\varepsilon_q^{(reg)}$ (left black axis) and of the of error metric $\varepsilon_q$ (right blue axis) on the regularization parameter $\mu$. These two values are combined in the L-curve. The red arrow and red dashed line indicate the regularization parameter selected for this trabecular bone sample as explained in the text.

A 3D visualization of the resulting SAXS tensor tomography reconstruction, corresponding to Fig. 10(a), is shown in Fig. 12(b). The reconstruction using both regularization of the coefficients, with a $5 \times 5 \times 5$ Hamming window as well as of the orientation with $\mu = 1 \times 10^{-3}$, is shown in 12(c). The reconstruction without regularization shows substantial noise particularly in the orientations, and no clear domains are visible. This variation is not supported by the measured data, as shown in projections from different sample orientations $(\alpha, \beta)$ in Fig. 12(a). The regularization with $\mu = 1 \times 10^{-3}$ as shown in (c) reduced the high-frequency noise without suppressing the different orientations found in the sample and leads to better defined regions of higher degree of orientation (light green). The sample contains different domains of orientation, each spanning some tens of micrometers, similar to the sample shown in Figs. 7 and 9. The higher resolution obtained here with a smaller beam size of $5 \times 1.4\,\mu m^2$ enables us to resolve the transition region between the domains.
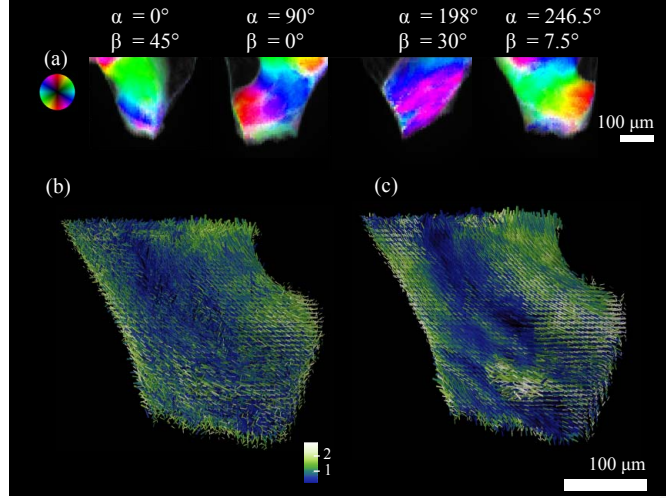
28



Fig. 12. Orientation of the bone ultrastructure from a human trabecular bone (Sample C). Four 2D SAXS projections at different sample orientations are shown in (a), where the color wheel represents the main scattering orientation, the hue the scattering intensity, and the degree of orientation the color saturation. The orientation of the bone ultrastructure retrieved from SAXS tensor tomography is shown in (b) and (c), where the color represents the degree of orientation and the length the isotropic component $a_0^0$. (b) Reconstruction without regularization applied and (c) with regularization of the spherical harmonics coefficients $a_l^m(\mathbf{r}', q')$ and on the direction $\hat{\mathbf{u}}_{\theta_{\mathrm{op}},\phi_{\mathrm{op}}}^{str}$ as described in the text.

## 6. Conclusion

SAXS tensor tomography aims at reconstructing the local 3D reciprocal-space map for each volume element within a 3D sample. This can be achieved through gradient-based optimization. An adequate numerical representation of the 3D reciprocal-space map, for which only a few quantities or coefficients have to be recovered for each voxel can be critical towards an approach that is efficient both in computational and measurement time. Liebi *et al.* (2015) introduced this reconstruction approach using spherical harmonics as a base to represent the reciprocal-space map and demonstrated it with a millimeter sized sample of trabecular bone. The 3D reciprocal-space map comprises information about the main orientation of the nanostructure for different

29

$q$-ranges and also its degree of orientation. The reciprocal-space map could be used further as input for fitting the underlying nanostructure in a similar way to what has been done on 2D SAXS data, for example to retrieve size parameters of the mineralized platelets in bone (Fratzl *et al.*, 2005; Turunen *et al.*, 2016).

In this manuscript we present a detailed description of the algorithm as well as a validation study to confirm the suitability of spherical harmonic coefficients to represent the 3D reciprocal-space map of trabecular bone where the features of the mineralized collagen fibrils can be recovered. In order to reduce the number of coefficients that need to be optimized we provide for each voxel a parametrization of the spherical harmonic zenith direction, which provides directly the orientation of the main symmetry axis of the nanostructure in 3D and subsequently allows us to impose reciprocal-space symmetry constraints. Regularization strategies for both the coefficients and the orientation are introduced and described in detail. An important consideration is the distribution of projection angles for the measurements. By selectively removing angles the effect on the reconstruction is shown, which confirms that a uniform distribution of sample orientations is of significant benefit for the reconstruction quality.

SAXS tensor tomography provides a technique that can probe 3D nanostructure information in relatively large volumes, offering the unique chance to correlate spatial nanoscale features over several millimeters, *i.e.* separated over five or six orders of magnitude. The technique is applicable to a wide range of specimens in biology and materials science and also scalable. While the original demonstration was with 20 micron voxel size, by using microfocusing optics and improved scanning hardware the current manuscript demonstrated the technique to a spatial resolution of 5 microns. By suitable changes in optics and hardware the resolution can be adjusted to the application of interest.

30

# Appendix A
## Analytical expressions for the gradients

The gradient of the error metric $\varepsilon_q$, as defined in equation 4, with respect to the spherical harmonic coefficients is given by

$$
\frac{\partial \varepsilon_q}{\partial a_l^m(\mathbf{r}', q)} = 4M(\mathbf{r}') \sum_{n,\phi} \omega_n(x, y, q, \phi)
$$

$$
\times \left[ \frac{\sqrt{\hat{I}_n(x, y, q, \phi)} - \sqrt{\dfrac{I_n(x, y, q, \phi)}{T_n(x, y)}}}{\sqrt{\hat{I}_n(x, y, q, \phi)}} \right] \tag{10}
$$

$$
\times Y_l^m \left( \Theta(\mathbf{r}', q)|_{\theta=\pi/2}, \Phi(\mathbf{r}', q)|_{\theta=\pi/2} \right)
$$

$$
\times \sum_{l',m'} a_{l'}^{m'}(\mathbf{r}', q) Y_{l'}^{m'} \left( \Theta(\mathbf{r}', q)|_{\theta=\pi/2}, \Phi(\mathbf{r}', q)|_{\theta=\pi/2} \right),
$$

where the notation $\Theta(\mathbf{r}', q)|_{\theta=\pi/2}$ indicates that the function is evaluated at the detector plane, $\theta = \pi/2$, in the laboratory coordinates $\mathbf{r}$, and with $q' = q$. Notice that the first term in brackets in equation 10 is only a function of $(x, y)$ in the laboratory coordinates $\mathbf{r}$ and that it is constant along the $z$ direction, which is effectively a back-projection. This is then computed *via* backprojection along the beam-propagation direction using bilinear interpolation.

The gradient with respect to $\theta_{\mathrm{op}}(\mathbf{r}', q)$ is given by

$$
\frac{\partial \varepsilon_q}{\partial \theta_{\mathrm{op}}(\mathbf{r}', q)} = 4M(\mathbf{r}') \sum_{n,\phi} \omega_n(x, y, q, \phi)
$$

$$
\times \left[ \frac{\sqrt{\hat{I}_n(x, y, q, \phi)} - \sqrt{\dfrac{I_n(x, y, q, \phi)}{T_n(x, y)}}}{\sqrt{\hat{I}_n(x, y, q, \phi)}} \right] \tag{11}
$$

$$
\times \left( \frac{\partial Y_l^m(\Theta, \Phi)}{\partial \Theta} \frac{\partial \, \Theta(\mathbf{r}', q)|_{\theta=\pi/2}}{\partial \theta_{\mathrm{op}}(\mathbf{r}', q)} \right.
$$

$$
\left. + \frac{\partial Y_l^m(\Theta, \Phi)}{\partial \Phi} \frac{\partial \, \Phi(\mathbf{r}', q)|_{\theta=\pi/2}}{\partial \theta_{\mathrm{op}}(\mathbf{r}', q)} \right)
$$

$$
\times \sum_{l',m'} a_{l'}^{m'}(\mathbf{r}', q) Y_{l'}^{m'} \left( \Theta(\mathbf{r}', q)|_{\theta=\pi/2}, \Phi(\mathbf{r}', q)|_{\theta=\pi/2} \right).
$$

31

The derivatives of the spherical harmonic functions are given by (Wolfram Research, 2017a; Wolfram Research, 2017b),

$$
\frac{\partial Y_l^m(\Theta, \Phi)}{\partial \Theta} = m Y_l^m(\Theta, \Phi) \cot \Theta
$$
$$
+ \sqrt{(l-m)(l+m+1)} \exp\left(-i\Phi\right) Y_l^{m+1}(\Theta, \Phi), \tag{12a}
$$
$$
\frac{\partial Y_l^m(\Theta, \Phi)}{\partial \Phi} = i m Y_l^m(\Theta, \Phi). \tag{12b}
$$

Using equation 2

$$
\frac{\partial\, \Theta(\mathbf{r}', q)|_{\theta=\pi/2}}{\partial \theta_{\mathrm{op}}(\mathbf{r}', q)} = \frac{1}{r' \sin \Theta(\mathbf{r}', q)|_{\theta=\pi/2}} \Big\{ z' \sin \theta_{\mathrm{op}}(\mathbf{r}', q)
$$
$$
- \left[ x' \cos \phi_{\mathrm{op}}(\mathbf{r}', q) + y' \sin \phi_{\mathrm{op}}(\mathbf{r}', q) \right] \cos \theta_{\mathrm{op}}(\mathbf{r}', q) \Big\} \Big|_{\theta=\pi/2}, \tag{13a}
$$
$$
\frac{\partial\, \Phi(\mathbf{r}', q)|_{\theta=\pi/2}}{\partial \theta_{\mathrm{op}}(\mathbf{r}', q)} = \cos^2 \Theta(\mathbf{r}', q)|_{\theta=\pi/2} \Big\{ - x'^2 \cos \phi_{\mathrm{op}}(\mathbf{r}', q)
$$
$$
- 2 y'^2 \cos \theta_{\mathrm{op}}(\mathbf{r}', q) \sin \theta_{\mathrm{op}}(\mathbf{r}', q) \sin \phi_{\mathrm{op}}(\mathbf{r}', q)
$$
$$
\times x' y' \sin \phi_{\mathrm{op}}(\mathbf{r}', q) \left[ \sin^2 \theta_{\mathrm{op}}(\mathbf{r}', q) - \cos^2 \theta_{\mathrm{op}}(\mathbf{r}', q) \right] + y' z' \Big\}
$$
$$
\Big/ \Big\{ x' \cos \theta_{\mathrm{op}}(\mathbf{r}', q) \cos \phi_{\mathrm{op}}(\mathbf{r}', q) + y' \cos \theta_{\mathrm{op}}(\mathbf{r}', q) \sin \phi_{\mathrm{op}}(\mathbf{r}', q)
$$
$$
- z' \sin \theta_{\mathrm{op}}(\mathbf{r}', q) \Big\}^2 \Big|_{\theta=\pi/2}, \tag{13b}
$$

Similarly, the gradient with respect to $\phi_{\mathrm{op}}(\mathbf{r}', q)$ is given by

$$
\frac{\partial \varepsilon_q}{\partial \phi_{\mathrm{op}}(\mathbf{r}', q)} = 4 M(\mathbf{r}') \sum_{n,\phi} \omega_n(x, y, q, \phi)
$$
$$
\times \left[ \frac{\sqrt{\hat{I}_n(x, y, q, \phi)} - \sqrt{\dfrac{I_n(x, y, q, \phi)}{T_n(x, y)}}}{\sqrt{\hat{I}_n(x, y, q, \phi)}} \right]
$$
$$
\times \left( \frac{\partial Y_l^m(\Theta, \Phi)}{\partial \Theta} \frac{\partial\, \Theta(\mathbf{r}', q)|_{\theta=\pi/2}}{\partial \phi_{\mathrm{op}}(\mathbf{r}', q)} \right. \tag{14}
$$
$$
\left. + \frac{\partial Y_l^m(\Theta, \Phi)}{\partial \Phi} \frac{\partial\, \Phi(\mathbf{r}', q)|_{\theta=\pi/2}}{\partial \phi_{\mathrm{op}}(\mathbf{r}', q)} \right)
$$
$$
\times \sum_{l',m'} a_{l'}^{m'}(\mathbf{r}', q) Y_{l'}^{m'}\left( \Theta(\mathbf{r}', q)|_{\theta=\pi/2}, \Phi(\mathbf{r}', q)|_{\theta=\pi/2} \right).
$$

with

$$\frac{\partial\,\Theta(\mathbf{r}',q)|_{\theta=\pi/2}}{\partial\phi_{\mathrm{op}}(\mathbf{r}',q)} = \frac{\sin\theta_{\mathrm{op}}(\mathbf{r}',q)}{r'\sin\Theta(\mathbf{r}',q)|_{\theta=\pi/2}}$$

$$\times\left[x'\sin\phi_{\mathrm{op}}(\mathbf{r}',q) - y'\cos\phi_{\mathrm{op}}(\mathbf{r}',q)\right]\Big|_{\theta=\pi/2}, \tag{15a}$$

$$\frac{\partial\,\Phi(\mathbf{r}',q)|_{\theta=\pi/2}}{\partial\theta_{\mathrm{op}}(\mathbf{r}',q)} = \cos^2\Theta(\mathbf{r}',q)|_{\theta=\pi/2}$$

$$\times\left[x'\sin\theta_{\mathrm{op}}(\mathbf{r}',q) - y'\cos\theta_{\mathrm{op}}(\mathbf{r}',q)\right]$$

$$\times\left[-x'\cos\theta_{\mathrm{op}}(\mathbf{r}',q)\sin\phi_{\mathrm{op}}(\mathbf{r}',q) + y'\cos\theta_{\mathrm{op}}(\mathbf{r}',q)\cos\phi_{\mathrm{op}}(\mathbf{r}',q)\right]$$

$$\Big/\left[x'\cos\theta_{\mathrm{op}}(\mathbf{r}',q)\cos\phi_{\mathrm{op}}(\mathbf{r}',q) + y\cos\theta_{\mathrm{op}}(\mathbf{r}',q)\sin\phi_{\mathrm{op}}(\mathbf{r}',q)\right.$$

$$\left. - z'\sin\theta_{\mathrm{op}}(\mathbf{r}',q)\right]^2\Big|_{\theta=\pi/2}, \tag{15b}$$

Using this gradient and the previous search direction a conjugate gradient direction is defined, and along this direction a linesearch is carried out to look for the minimum value of the error metric (Press *et al.*, 2007).

If the smooth penalty term $\varepsilon_q^{(p)}$ is introduced in the error metric as described in equations 5 and 6, the gradient of the error metric with respect to the spherical harmonic coefficients (equation 10) is

$$\frac{\partial\varepsilon_q'}{\partial a_l^m(\mathbf{r}',q)} = \frac{\partial\varepsilon_q}{\partial a_l^m(\mathbf{r}',q)} + \lambda\frac{\partial\varepsilon_q^{(p)}}{\partial a_l^m(\mathbf{r}',q)} \tag{16}$$

with

$$\frac{\partial\varepsilon_q^{(p)}}{\partial a_l^m(\mathbf{r}',q)} = \sum_{\mathbf{r}'}\begin{cases} 2[a_l^m(\mathbf{r}',q) - c], & \text{if } a_l^m(\mathbf{r}',q) < c, \\ 0 & \text{otherwise} \end{cases} \tag{17}$$

If regularization of the local preferential orientation $\hat{\mathbf{u}}_{\theta_{\mathrm{op}},\phi_{\mathrm{op}}}^{\mathrm{str}}(\mathbf{r}',q)$ is used, the gradient with respect to $\theta_{\mathrm{op}}(\mathbf{r}',q)$ is

$$\frac{\partial\varepsilon_q'}{\partial\theta_{\mathrm{op}}(\mathbf{r}',q)} = \frac{\partial\varepsilon_q}{\partial\theta_{\mathrm{op}}(\mathbf{r}',q)} + \mu\frac{\partial\varepsilon_q^{(reg)}}{\partial\theta_{\mathrm{op}}(\mathbf{r}',q)} \tag{18}$$

33

with

$$\frac{\partial \varepsilon_q^{(reg)}}{\partial \theta_{\text{op}}(\mathbf{r}',q)} = \sum_{\mathbf{r}'} \left[ -\frac{\partial \left| \hat{\mathbf{u}}_{\theta_{\text{op}},\phi_{\text{op}}}^{\text{str}}(\mathbf{r}',q) \cdot \hat{\mathbf{u}}_{\theta_{\text{op}},\phi_{\text{op}}}^{\text{str}}(\mathbf{r}'+\hat{i}\delta,q) \right|}{\partial \theta_{\text{op}}(\mathbf{r}',q)} \right.$$
$$-\frac{\partial \left| \hat{\mathbf{u}}_{\theta_{\text{op}},\phi_{\text{op}}}^{\text{str}}(\mathbf{r}',q) \cdot \hat{\mathbf{u}}_{\theta_{\text{op}},\phi_{\text{op}}}^{\text{str}}(\mathbf{r}'+\hat{j}\delta,q) \right|}{\partial \theta_{\text{op}}(\mathbf{r}',q)} \tag{19}$$
$$\left. -\frac{\partial \left| \hat{\mathbf{u}}_{\theta_{\text{op}},\phi_{\text{op}}}^{\text{str}}(\mathbf{r}',q) \cdot \hat{\mathbf{u}}_{\theta_{\text{op}},\phi_{\text{op}}}^{\text{str}}(\mathbf{r}'+\hat{k}\delta,q) \right|}{\partial \theta_{\text{op}}(\mathbf{r}',q)} \right],$$

with

$$\frac{\partial \left| \hat{\mathbf{u}}_{\theta_{\text{op}},\phi_{\text{op}}}^{\text{str}}(\mathbf{r}',q) \cdot \hat{\mathbf{u}}_{\theta_{\text{op}},\phi_{\text{op}}}^{\text{str}}(\mathbf{r}'+\hat{i}\delta,q) \right|}{\partial \theta_{\text{op}}(\mathbf{r}',q)} =$$
$$\frac{\hat{\mathbf{u}}_{\theta_{\text{op}},\phi_{\text{op}}}^{\text{str}}(\mathbf{r}',q) \cdot \hat{\mathbf{u}}_{\theta_{\text{op}},\phi_{\text{op}}}^{\text{str}}(\mathbf{r}'+\hat{i}\delta,q)}{\left| \hat{\mathbf{u}}_{\theta_{\text{op}},\phi_{\text{op}}}^{\text{str}}(\mathbf{r}',q) \cdot \hat{\mathbf{u}}_{\theta_{\text{op}},\phi_{\text{op}}}^{\text{str}}(\mathbf{r}'+\hat{i}\delta,q) \right|}$$
$$\times \left[ \cos\left(\phi_{\text{op}}(\mathbf{r}',q) + \phi_{\text{op}}(\mathbf{r}'+\hat{i}\delta,q)\right) \cos \theta_{\text{op}}(\mathbf{r}',q) \right. \tag{20}$$
$$\times \sin \theta_{\text{op}}(\mathbf{r}'+\hat{i}\delta,q) + \cos\left(\phi_{\text{op}}(\mathbf{r}',q) + \phi_{\text{op}}(\mathbf{r}'-\hat{i}\delta,q)\right)$$
$$\times \sin \theta_{\text{op}}(\mathbf{r}'-\hat{i}\delta,q) \cos \theta_{\text{op}}(\mathbf{r}',q) + \left(-\sin \theta_{\text{op}}(\mathbf{r}',q)\right.$$
$$\left. \times \cos \theta_{\text{op}}(\mathbf{r}'+\hat{i}\delta,q) - \cos \theta_{\text{op}}(\mathbf{r}'-\hat{i}\delta,q) \sin \theta_{\text{op}}(\mathbf{r}',q) \right].$$

Similarly, expressions for the terms with finite differences in the $y$ and $z$ direction can be obtained to complete equation 19. Equivalent expressions can be found for the gradient with respect to $\phi_{\text{op}}(\mathbf{r}',q)$.

## Appendix B
## Experimental Details

*B.1. Sample preparation*

Trabeculas from a twelfth thoracic (T12) human vertebra from a 50 year old woman (sample A) and a 73 year old man (samples B and C) were extracted and soft tissue

34

was removed before embedding into polymethyl methacrylate (PMMA). The vertebrae were obtained from the Department of Anatomy, Histology, and Embryology at the Innsbruck Medical University, Innsbruck, Austria, with the written consent of the donors according to Austrian law. All following procedures were performed in accordance with Swiss law, the Guideline on Bio-Banking of the Swiss Academy of the Medical Science (2006), and the Swiss ordinance 814.912 (2012) on the contained use of organisms. To obtain sample A, a 20 µm thick section was cut using a microtome (HM 355S; Thermo Fisher Scientific Inc. USA) and mounted on 12 µm thick Kapton adhesive tape (T2000023; Benetec, Wettswil, Switzerland). A cylinder of about 1 mm and 250 µm diameter was milled out of the PMMA block for samples B and C, respectively.

### B.2. Experiments

Measurements were performed at the coherent small-angle X-ray scattering (cSAXS) beamline (X12SA) of the Swiss Light Source, Paul Scherrer Institut, Switzerland. The X-ray beam was monochromatized by a fixed-exit double-crystal Si(111) monochromator to 12.4 keV for samples A and B, and to 11.2 keV X-ray energy for sample C. Two different types of focusing were used. For samples A and B the beam was focused horizontally by bending the second monochromator crystal and vertically by bending a Rh-coated mirror resulting in a beamsize of about $20 \times 20 \, \mu m^2$ and $25 \times 25 \, \mu m^2$, respectively. For sample C the beam was focused with a Fresnel zone plate to a beamsize of $5 \times 1.4 \, \mu m^2$ (Lebugle *et al.*, 2017). To minimize air scattering and X-ray absorption a 7 m (sample A and B) or a 2 m long (sample C) flight tube was placed between sample and detector. X-ray scattering was measured with a Pilatus 2M detector (Kraft *et al.*, 2009) and the transmitted beam intensity with a photo-diode mounted on a beamstop placed inside the flight tube.

35

Sample A, a thin section of trabecular bone, was measured in the 3D scanning SAXS setup as described in Georgiadis *et al.* (2015) and schematically shown in Fig. 1a. The sample was mounted on a goniometer placed on a rotation stage on top of a two-axis translation stage. The sample was continuously moved in $x$-direction while SAXS patterns were measured with 50 ms exposure time. The scan was repeated at 30 different sample orientations around the $y$-axis in steps of $10°$, omitting the angles where the section was close to parallel to the X-ray beam, i.e. $80 - 100°$ and $260 - 280°$. The scan step in $x$ was chosen to be $20\cos(\beta)$µm to have a consistent number of scanning points across the specimen. The scan step in $y$ was $20$ µm. To identify the scattering that originates from a specific voxel under all sample rotation angles, image registration (Guizar-Sicairos *et al.*, 2008) on the transmission images was used, as described in detail in Georgiadis *et al.* (2015).

Samples B and C were measured with the 3D tensor tomography setup as described in Liebi *et al.* (2015) and schematically shown in Fig. 1b. The sample was mounted on a goniometer on two perpendicular rotation stages which were placed on a two-axis scanning stage.

Sample B was measured at $n = 240$ projections, each with $55 \times 65$ scanning steps with a step-size of $25$ µm. The sample was continuously moved in $x$-direction while SAXS patterns were measured with an exposure time of $30$ ms, which was limited by the detector read-out. The angular spacing was $15°$ between $-30°$ and $45°$ in $\beta$ and $4.5°$ between $0°$ and $180°$ in $\alpha$. The total exposure time was $8.3$ h. Each voxel was exposed for a total of $7.2$ s. Due to overhead from motor movement, the total measurement time was $20.3$ h.

Sample C was measured at $n = 333$ projections, each with $85 \times 65$ scanning steps with a step size of $5$ µm and an exposure time of $50$ ms. As the beam in vertical $(y)$ was smaller than the step size, the sample was continuously moved in $y$-direction during

36

measurement in order to probe the whole sample volume. Based on our findings with regard to the advantage of an even distribution of projection angles $\Delta\beta = 7.5°$ and $\Delta\alpha = 7.5° \cos(\beta)$ have been used. The total exposure time was 11.8 h and the total measurement time 21.3 h. The overhead of motor movements was reduced compared to the measurement of sample B, mainly by introducing a snake-like scan pattern where subsequent lines are scanned in opposite directions, which reduces the time the motor needs to reach the line scan starting position. Additional projections were measured at $\beta = 0$, achieving $\Delta\alpha = 3°$ to have enough projections for the standard filtered backprojection reconstruction used for image registration as described in section 5.

## Appendix B
## Acknowledgements

## Appendix B
## Funding information

## Availability of the software

A current version of the data analysis software is available upon request to the corresponding authors.

# References

Belge, M., Kilmer, Misha, E. & Miller, Eric, L. (2002). *Inverse Probl.* **18**(4), 1161.
  *http://stacks.iop.org/IP/18/1161

Beniash, E. (2011). *WIREs Nanomed. Nanobiotechnol.* **3**(1), 47–69.
  *http://dx.doi.org/10.1002/wnan.105

Bressler, I., Kohlbrecher, J. & Thunemann, A. F. (2015). *J. Appl. Cryst.* **48**(5), 1587–1598.
  *https://doi.org/10.1107/S1600576715016544

Bunge, H. J. & Roberts, W. T. (1969). *J. Appl. Cryst.* **2**(3), 116–128.
  *http://dx.doi.org/10.1107/S0021889869006704

Bunk, O., Bech, M., Jensen, T. H., Feidenhans'l, R., Binderup, T., Menzel, A. & Pfeiffer, F.
  (2009). *New J. Phys.* **11**.
  *http://dx.doi.org/10.1088/1367-2630/11/12/123016

Feldkamp, J. M., Kuhlmann, M., Roth, S. V., Timmann, A., Gehrke, R., Shakhverdova, I.,
  Paufler, P., Filatov, S. K., Bubnova, R. S. & Schroer, C. G. (2009). *Phys. Status Solidi*,
  **206**(8), 1723–1726.
  *http://dx.doi.org/10.1002/pssa.200881615

Fratzl, P., Fratzl-Zelman, N., Klaushofer, K., Vogl, G. & Koller, K. (1991). *Calcif. Tissue Int.*
  **48**(6), 407–413.
  *http://dx.doi.org/10.1007/BF02556454

Fratzl, P., Gupta, H. S., Paris, O., Valenta, A., Roschger, P. & Klaushofer, K. (2005). *Diffract-
  ing stacks of cards - some thoughts about small-angle scattering from bone*, pp. 33–39.
  Berlin, Heidelberg: Springer Berlin Heidelberg.
  *https://doi.org/10.1007/b107343

Fratzl, P., Jakob, H. F., Rinnerthaler, S., Roschger, P. & Klaushofer, K. (1997). *J. Appl. Cryst.*
  **30**(5 Part 2), 765–769.
  *http://dx.doi.org/10.1107/S0021889897001775

Fratzl, P. & Weinkamer, R. (2007). *Prog. Mater. Sci.* **52**(8), 1263–1334.
  *http://dx.doi.org/10.1016/j.pmatsci.2007.06.001

Georgiadis, M., Guizar-Sicairos, M., Gschwend, O., Hangartner, P., Bunk, O., Mller, R. &
  Schneider, P. (2016). *PLoS ONE*, **11**(8), e0159838.
  *http://dx.doi.org/10.13712Fjournal.pone.0159838

Georgiadis, M., Guizar-Sicairos, M., Zwahlen, A., Trssel, A. J., Bunk, O., Mller, R. & Schnei-
  der, P. (2015). *Bone*, **71**(0), 42–52.
  *http://dx.doi.org/10.1016/j.bone.2014.10.002

Giannini, C., Siliqi, D., Ladisa, M., Altamura, D., Diaz, A., Beraudi, A., Sibillano, T., De Caro,
  L., Stea, S., Baruffaldi, F. & Bunk, O. (2014). *J. Appl. Cryst.* **47**(1), 110–117.
  *http://dx.doi.org/10.1107/S1600576713030215

Gourrier, A., Li, C. H., Siegel, S., Paris, O., Roschger, P., Klaushofer, K. & Fratzl, P. (2010).
  *J. Appl. Cryst.* **43**, 1385–1392.
  *http://dx.doi.org/10.1107/s0021889810035090

Granke, M., Gourrier, A., Rupin, F., Raum, K., Peyrin, F., Burghammer, M., Saed, A. &
  Laugier, P. (2013). *PLoS ONE*, **8**(3), e58043.
  *http://dx.doi.org/10.13712Fjournal.pone.0058043

Grenander, U. (1981). *Abstract Inference.* New York: Wiley.

Guizar-Sicairos, M., Thurman, S. T. & Fienup, J. R. (2008). *Opt. Lett.* **33**(2), 156–158.
  *http://dx.doi.org/10.1364/OL.33.000156

Hansen, P. C. (1992). *SIAM Rev.* **34**(4), 561–580.
  *http://dx.doi.org/10.1137/1034115

He, W.-X., Rajasekharan, A. K., Tehrani-Bagha, A. R. & Andersson, M. (2015). *Adv. Mater.*
  **27**(13), 2260–2264.
  *http://dx.doi.org/10.1002/adma.201404926

Jackson, J. D. (1999). *Classical electrodynamics*. New York, NY: Wiley, 3rd ed.
  *http://cdsweb.cern.ch/record/490457

Jensen, T. H., Bech, M., Bunk, O., Thomsen, M., Menzel, A., Bouchet, A., Le Duc, G.,
  Feidenhans'l, R. & Pfeiffer, F. (2011). *Phys. Med. Biol.* **56**(6), 1717–1726.
  *http://dx.doi.org/10.1088/0031-9155/56/6/012

Kraft, P., Bergamaschi, A., Broennimann, C., Dinapoli, R., Eikenberry, E. F., Henrich, B.,
  Johnson, I., Mozzanica, A., Schleputz, C. M., Willmott, P. R. & Schmitt, B. (2009). *J.
  Synchrotron Radiat.* **16**(3), 368–375.
  *http://dx.doi.org/10.1107/S0909049509009911

Lebugle, M., Liebi, M., Wakonig, K., Guzenko, V. A., Holler, M., Menzel, A., Guizar-Sicairos,
  M., Diaz, A. & David, C. (2017). *Opt. Express*, **25**(18), 21145–21158.
  *https://doi.org/10.1364/OE.25.021145

Li, A., Miller, E. L., Kilmer, M. E., Brukilacchio, T. J., Chaves, T., Stott, J., Zhang, Q., Wu,
  T., Chorlton, M., Moore, R. H., Kopans, D. B. & Boas, D. A. (2003). *Appl. Opt.* **42**(25),
  5181–5190.
  *http://dx.doi.org/10.1364/AO.42.005181

Liebi, M., Georgiadis, M., Menzel, A., Schneider, P., Kohlbrecher, J., Bunk, O. & Guizar-
  Sicairos, M. (2015). *Nature*, **527**(7578), 349–52.
  *http://dx.doi.org/10.1038/nature16056

Liu, Y. F., Manjubala, I., Roschger, P., Schell, H., Duda, G. N. & Fratzl, P. (2010). *Xiv
  International Conference on Small-Angle Scattering (Sas09)*, **247**, 9.
  *http://dx.doi.org/10.1088/1742-6596/247/1/012031

Meyers, M. A., Chen, P.-Y., Lin, A. Y.-M. & Seki, Y. (2008). *Prog. Mater. Sci.* **53**(1), 1–206.
  *http://dx.doi.org/10.1016/j.pmatsci.2007.05.002

Norio, M., Morio, A. & Yoshio, T. (1982). *Jpn. J. Appl. Phys.* **21**(1R), 186.
  *http://dx.doi.org/10.1143/jjap.21.186

Pabisch, S., Wagermaier, W., Zander, T., Li, C. H. & Fratzl, P. (2013). *Imaging the Nanos-
  tructure of Bone and Dentin Through Small- and Wide-Angle X-Ray Scattering*, vol. 532,
  pp. 391–413. San Diego: Elsevier Academic Press Inc.
  *http://dx.doi.org/10.1016/b978-0-12-416617-2.00018-7

Press, W. H., Teukolsky, S. A., Vetterling, W. T. & Flannery, B. P. (2007). *Numerical Recipes
  3rd Edition: The Art of Scientific Computing*. Cambridge University Press.

Rinnerthaler, S., Roschger, P., Jakob, H. F., Nader, A., Klaushofer, K. & Fratzl, P. (1999).
  *Calcif. Tissue Int.* **64**(5), 422–429.
  *http://dx.doi.org/10.1007/PL00005824

Roe, R. & Krigbaum, W. R. (1964). *J. Chem. Phys.* **40**(9), 2608–2615.
  *http://dx.doi.org/10.1063/1.1725571

Santos, E. T. F. & Bassrei, A. (2007). *Comput. Geosci.* **33**(5), 618–629.
  *http://dx.doi.org/10.1016/j.cageo.2006.08.013

Schaff, F., Bech, M., Zaslansky, P., Jud, C., Liebi, M., Guizar-Sicairos, M. & Pfeiffer, F. (2015).
  *Nature*, **527**(7578), 353–6.
  *http://dx.doi.org/10.1038/nature16060

Schroer, C. G., Kuhlmann, M., Roth, S. V., Gehrke, R., Stribeck, N., Almendarez-Camarillo,
  A. & Lengeler, B. (2006). *Appl. Phys. Lett.* **88**(16), –.
  *http://dx.doi.org/10.1063/1.2196062

Seidel, R., Gourrier, A., Kerschnitzki, M., Burghammer, M., Fratzl, P., Gupta, H. S. & Wager-
  maier, W., (2012). Synchrotron 3d saxs analysis of bone nanostructure.
  *http://dx.doi.org/10.1680/bbn.11.00014

Skjonsfjell, E. T., Kringeland, T., Granlund, H., Hoydalsvik, K., Diaz, A. & Breiby, D. W.
  (2016). *J. Appl. Cryst.* **49**(3), 902–908.
  *https://doi.org/10.1107/S1600576716005574

Thibault, P. & Guizar-Sicairos, M. (2012). *New J. Phys.* **14**(6), 063004.
  *http://dx.doi.org/10.1088/1367-2630/14/6/063004

39

Tinti, G., Bergamaschi, A., Cartier, S., Dinapoli, R., Greiffenberg, D., Johnson, I., Jungmann-Smith, J. H., Mezza, D., Mozzanica, A., Schmitt, B. & Shi, X. (2015). *J. Instrum.* **10**(03), C03011.
*http://dx.doi.org/10.1088/1748-0221/10/03/C03011

Turunen, M. J., Kaspersen, J. D., Olsson, U., Guizar-Sicairos, M., Bech, M., Schaff, F., Tgil, M., Jurvelin, J. S. & Isaksson, H. (2016). *J. Struct. Biol.* **195**(3), 337–344.
*http://dx.doi.org/10.1016/j.jsb.2016.07.005

Van Houtte, P. (1983). *Textures and Microstructures*, **6**(1), 1–19.
*http://dx.doi.org/10.1155/TSM.6.1

Van Opdenbosch, D., Fritz-Popovski, G., Wagermaier, W., Paris, O. & Zollfrank, C. (2016). *Adv. Mater.* **28**(26), 5235–5240.
*http://dx.doi.org/10.1002/adma.201600117

Wilkinson, S. J. & Hukins, D. W. L. (1999). *Radiat. Phys. and Chem.* **56**(12), 197–204.
*http://dx.doi.org/10.1016/S0969-806X(99)00282-0

Wolfram Research, I., (2017*a*).
*http://functions.wolfram.com/05.10.20.0001.01

Wolfram Research, I., (2017*b*).
*http://functions.wolfram.com/05.10.20.0005.01